

Influence of crystal dimension on performance of spherical crystal self-emission imager

Chenglong Zhang(张成龙), Yihang Zhang(张翌航), Haochen Gu(谷昊琛), Nuo Chen(陈诺), Xiaohui Yuan(远晓辉), Zhe Zhang(张喆), Miaohua Xu(徐妙华), Yutong Li(李玉同), Yingjun Li(李英骏), and Jie Zhang(张杰)

Citation: Chin. Phys. B, 2024, 33 (**12**): 125205. DOI: 10.1088/1674-1056/ad84d2
Journal homepage: http://cpb.iphy.ac.cn; http://iopscience.iop.org/cpb

What follows is a list of articles you may be interested in

Spectral characteristics of laser-plasma instabilities with a broadband laser

Guo-Xiao Xu(许国潇), Ning Kang(康宁), An-Le Lei(雷安乐), Hui-Ya Liu(刘会亚), Yao Zhao(赵耀), Shen-Lei Zhou(周申蕾), Hong-Hai An(安红海), Jun Xiong(熊俊), Rui-Rong Wang(王瑞荣), Zhi-Yong Xie(谢志勇), Xi-Chen Zhou(周熙晨), Zhi-Heng Fang(方智恒), and Wei Wang(王伟)

Chin. Phys. B, 2024, 33 (**8**): 085204. DOI: 10.1088/1674-1056/ad426d

Velocity analysis of supersonic jet flow in double-cone ignition scheme

Zhong-Yuan Zhu(朱仲源), Cheng-Long Zhang(张成龙), and Ying-Jun Li(李英骏)

Chin. Phys. B, 2024, 33 (**6**): 065203. DOI: 10.1088/1674-1056/acc1d4

Development of a monochromatic crystal backlight imager for the recent double-cone ignition experiments

Chenglong Zhang(张成龙), Yihang Zhang(张翌航), Xiaohui Yuan(远晓辉), Zhe Zhang(张喆), Miaohua Xu(徐妙华), Yu Dai(戴羽), Yufeng Dong(董玉峰), Haochen Gu(谷昊琛), Zhengdong Liu(刘正东), Xu Zhao(赵旭), Yutong Li(李玉同), Yingjun Li(李英骏), Jianqiang Zhu(朱健强), and Jie Zhang(张杰)

Chin. Phys. B, 2024, 33 (**2**): 025201. DOI: 10.1088/1674-1056/ad1091

Simulations of hot electron transport in radiation-ablated plasma

Bin Zhao(赵斌), Tao Tao(陶弢), Rui Yan(闫锐), and Jian Zheng(郑坚)

Chin. Phys. B, 2023, 32 (**8**): 085201. DOI: 10.1088/1674-1056/acc0f3

Influence analysis of symmetry on capsule in six-cylinder-port hohlraum

You Zou(邹游), Wudi Zheng(郑无敌), Xin Li(李欣)

Chin. Phys. B, 2019, 28 (**3**): 035203. DOI: 10.1088/1674-1056/28/3/035203

INSTRUMENTATION AND MEASUREMENT

Influence of crystal dimension on performance of spherical crystal self-emission imager

Chenglong Zhang(张成龙)[1,2], Yihang Zhang(张翌航)[2], Haochen Gu(谷昊琛)[2,3], Nuo Chen(陈诺)[2,3], Xiaohui Yuan(远晓辉)[4,5], Zhe Zhang(张喆)[2,5,6,†], Miaohua Xu(徐妙华)[7,‡], Yutong Li(李玉同)[2,5,6], Yingjun Li(李英骏)[1,§], and Jie Zhang(张杰)[2,4,5]

[1] *State Key Laboratory for Tunnel Engineering, China University of Mining and Technology, Beijing* 100083, *China*
[2] *Beijing National Laboratory for Condensed Matter Physics, Institute of Physics, Chinese Academy of Sciences, Beijing* 100190, *China*
[3] *School of Physical Sciences, University of Chinese Academy of Sciences, Beijing* 100049, *China*
[4] *Key Laboratory for Laser Plasmas (MoE) and School of Physics and Astronomy, Shanghai Jiao Tong University, Shanghai* 200240, *China*
[5] *Collaborative Innovation Center of IFSA (CICIFSA), Shanghai Jiao Tong University, Shanghai* 200240, *China*
[6] *Songshan Lake Materials Laboratory, Dongguan* 523808, *China*
[7] *School of Science, China University of Mining and Technology (Beijing), Beijing* 100089, *China*

(Received 9 September 2024; revised manuscript received 20 September 2024; accepted manuscript online 9 October 2024)

The spherical crystal imaging system, noted for its high energy spectral resolution (monochromaticity) and spatial resolution, is extensively applied in high energy density physics and inertial confinement fusion research. This system supports studies on fast electron transport, hydrodynamic instabilities, and implosion dynamics. The x-ray source, produced through laser–plasma interaction, emits a limited number of photons within short time scales, resulting in predominantly photon-starved images. Through ray-tracing simulations, we investigated the impact of varying crystal dimensions on the performance of a spherical crystal self-emission imager. We observed that increasing the crystal dimension leads to higher imaging efficiency but at the expense of monochromaticity, causing broader spectral acceptance and reduced spatial resolution. Furthermore, we presented a theoretical model to estimate the spatial resolution of the imaging system within a specific energy spectrum range, detailing the expressions for the effective size of the crystal. The spatial resolution derived from the model closely matches the numerical simulations.

Keywords: crystal dimensions, self-emission imager, x-ray radiography

PACS: 52.57.–z, 52.57.Kk **DOI:** 10.1088/1674-1056/ad84d2

1. Introduction

X-ray imaging with spherical crystals relies on Bragg diffraction of x-rays from crystal planes. Specific x-rays are reflected by the crystal lattice according to the Bragg condition, which is given by $2d\sin\theta = n\lambda$. Here λ is the x-ray wavelength, n denotes the reflection order, d is the lattice spacing of the crystal, and θ the grazing angle (Bragg angle). The spherical crystal, conforming to Coddington's equations in its focusing behavior, produces a spectral reflection that creates an image reminiscent of a traditional optical mirror.[1] The interest in spherical crystals imaging, initially demonstrated in the 1970s[2] and known for its high energy spectral and spatial resolution, has led to its extensive exploration in numerous experiments,[3,4] particularly in high energy density physics and inertial confinement fusion (ICF).[5–8] In addition to improvements in mechanical structures and other aspects, recent advancements in x-ray crystal imaging have primarily focused on the selection of x-ray sources. Characteristic spectral lines, such as $K\alpha$ lines from picosecond lasers and helium-like lines from nanosecond lasers, are commonly used as x-ray sources in experiments.[9,10] At this stage, various x-ray spherical crystal imaging systems have been developed, including backlighter systems[11,12] based on Si-Heα, Cl-Heα, V-Heα, Mn-Heα, Se-Heα, Cu-$K\alpha$, and Ti-$K\alpha$. These systems are used to investigate hydrodynamic instability[13] during ablation and implosion dynamics[14] at the final stage of ignition compression. Additionally, Cu-$K\alpha$ and Ti-$K\alpha$ based self-emission imagers have been utilized to study fast electrons produced by laser–plasma interactions, focusing on their transport,[15] energy deposition,[16,17] divergence,[18,19] and resistive collimation.[20]

The interaction between laser and plasma generates an x-ray source that emits a limited number of photons within a short period (nanoseconds or picoseconds). For example, when a 500 J, 10 ps laser beam interacts with a copper target, it produces approximately 10^{11} $K\alpha$ photons per unit solid angle. Considering the limited diffraction efficiency and the collection angle of the crystal, most images are photon-starved.

†Corresponding author. E-mail: zzhang@iphy.ac.cn
‡Corresponding author. E-mail: mhxu@cumtb.edu.cn
§Corresponding author. E-mail: lyj@aphy.iphy.ac.cn

© 2024 Chinese Physical Society and IOP Publishing Ltd

Increasing the crystal dimension effectively enhances the image brightness in self-emission imagers. The effective size of the crystal influences the field of view, image fluence, spectral acceptance, and spatial resolution of the spherical crystal self-emitting imager. Although the existing literature[21,22] has discussed the difference between the geometric and effective crystal dimensions, the precise relationship between the effective dimension, geometric dimension, and energy spectrum width remains unclear. This paper presents the first systematic study on how crystal dimension affects the performance (image fluence, monochromaticity, and spatial resolution) of a spherical crystal self-emission imager.

2. Simulation parameter settings in OASYS

Considering the geometry of the Shenguang-II upgrade facility chamber[23] and the requirements of the double-cone ignition scheme,[24] we developed a self-emission imager featuring the quartz (2131) spherical crystal with two radii of curvature: $R = 200$ mm and $R = 400$ mm. OASYS (OrAnge SYnchrotron Suite)[25] is an open-source graphical platform designed for x-ray virtual experiments, supporting extensive ray-tracing simulations, such as mirrors, crystals, gratings, slits, etc. Physical models of crystal optics in ray-tracing procedures have been summarized and the applicability of ray-tracing methods in the design and optimization of x-ray crystal optics has been demonstrated. Various x-ray crystal diagnostics are designed and optimized using OASYS.[26,27] At present, OASYS simulates a limited number of rays, which is not conducive to calculating crystals with low diffraction efficiencies, and can only perform two-dimensional simulations. The work of this paper is not affected by these two factors. Using OASYS ray-tracking simulations, we assessed how crystal dimension influences the performance of self-emission imager at two different radii of curvature. The parameters of the imaging system, including the radius of curvature (R), object distance (p), image distance (q), and magnification (M), are detailed in Table 1.

Table 1. Imaging parameters used in the simulation.

R (mm)	200	400
p (mm)	106.3	224.9
q (mm)	1686.1	1804.4
M	15.8	8.0

The simulations utilize x-ray sources with a Gaussian beam profile (with FWHM of 100 μm), as illustrated in Fig. 1(a), and a uniform divergence angle of ±0.4 radians. Figure 1(a) is a schematic of the self-emission imager in the simulation, where D is the crystal dimension. The x-ray beamline is directed toward the crystal and subsequently detected after diffraction. To enhance the number of x-ray photons in the simulation, a cycle storage module has been implemented to accumulate and direct more rays toward the crystal for imaging, with a three-million photon count set for this simulation. We performed simulations using monoenergetic x-ray sources at 8048 eV and 8068 eV. Furthermore, x-ray sources with energy spectra measured by HOPG crystal spectrometer[28] in picosecond laser and copper interaction experiments were also employed in the simulations, as depicted in Fig. 1(b).

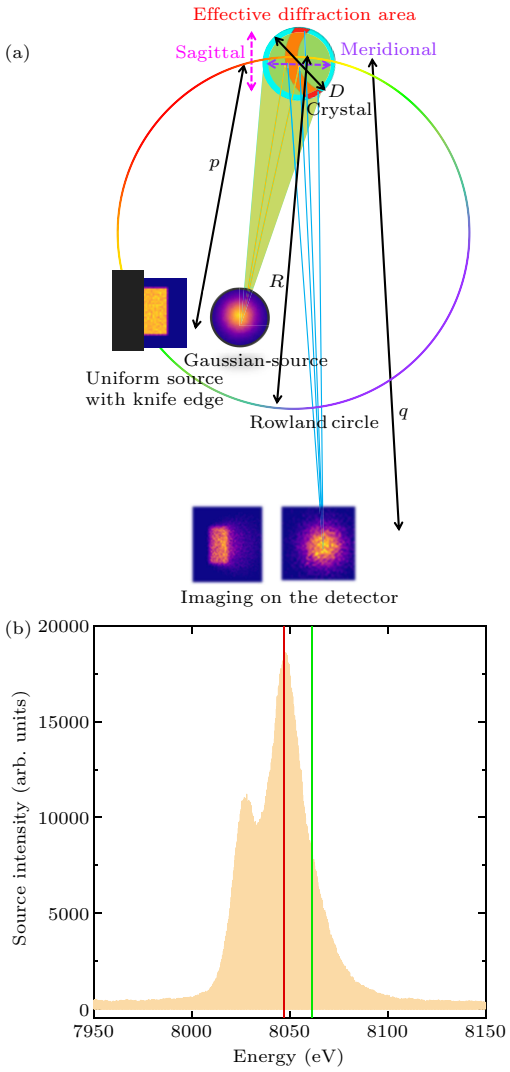


Fig. 1. (a) Schematic diagram of the self-emission imager in the simulation. (b) Energy spectrum distribution of the x-ray source obtained from measurements with HOPG spectrometer in the experiment, where the red and green lines indicate 8048 eV and 8068 eV, respectively.

3. Effect of crystal dimension on image fluence

The experimentally measured Cu-$K\alpha$ energy spectrum (Fig. 1(b)) exhibits a peak at 8048 eV, corresponding to a diffraction angle of 88.12° for the quartz (2131) crystal. In all the subsequent simulations, the center of the crystal was aligned with the 8048 eV diffraction position. For $R = 200$ mm and $R = 400$ mm, the effective diffraction regions for varying energies and crystal dimensions are illustrated in Figs. 2 and 3, respectively. The X-axis denotes the meridional direction, while the Y-axis represents the sagittal direction. The results

for x-ray sources with monoenergetic energies of 8048 eV, 8068 eV, and with the experimental spectrum (ES) are illustrated. It can be observed in Fig. 2 that the diffraction area gradually increases, and then reaches the maximum and gets stabilized, as the crystal dimension increases, according to the maximum photon diffraction. For x-ray sources with individual energy, the width of the diffraction ring is determined by the diffraction curve of the quartz crystal. In the case of the ES spectrum, the width of the diffraction region is mainly determined by the diffractive energy range.

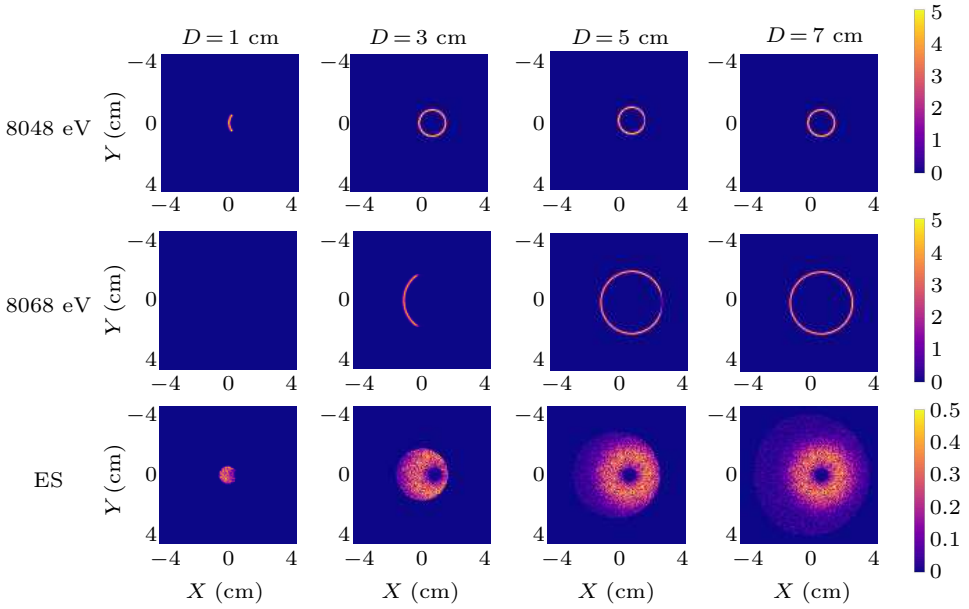


Fig. 2. Effective diffraction regions for different energies with different crystal dimensions for $R = 200$ mm. Here D indicates the dimension of the quartz crystal.

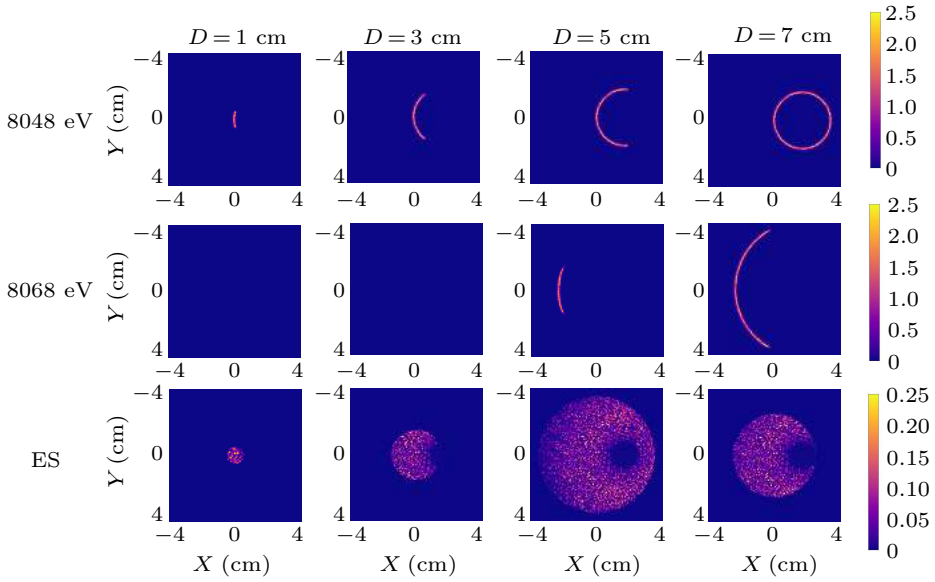


Fig. 3. Effective diffraction regions for different energies with different crystal dimensions for $R = 400$ mm.

As depicted in Fig. 4, the diffractable energy range varies with the crystal dimension. Smaller crystals can achieve quasi-monoenergetic images. For instance, at $D = 3$ cm, the x-ray energy range collected is approximately 30 eV, which narrows to about 10 eV at $D = 1$ cm (see Fig. 4(a)). The energy range that the crystal can diffract becomes broader as the crystal dimension increases. For crystals with the same dimension at $R = 400$ mm, monochromaticity improves compared to $R = 200$ mm (see Fig. 4(b)).

Furthermore, the simulation results reveal a correlation between the photon counts and peak intensity with crystal dimension. We investigate the trends in image fluence across varying crystal dimensions, with Fig. 5 showing different conditions: black scatter for 8048 eV, red scatter for 8068 eV, and green scatter for the experimental spectrum. In Fig. 5(a), the photon count at 8048 eV saturates at $D = 3$ cm, approximately 10 times higher than that at $D = 1$ cm. Saturation for 8068 eV occurs around $D = 6$ cm. Figure 5(b) demonstrates

that for $R = 400$ mm, the photon count of 8048 eV saturates at $D = 7$ cm, which is consistent with Fig. 3, where the photon count is about 11 times higher than that at $D = 1$ cm. Figure 5(c) illustrates how the peak intensity of the image varies with crystal dimension when the experimental spectrum is used for the x-ray source. The magnification of the imaging system is taken into account for the peak intensity of the R400-ES in Fig. 5(c) to be higher than that of the R200-ES. For a crystal with $R = 200$ mm, while the total photon count on the detector continues to increase steadily, the peak intensity saturates beyond a crystal dimension of 5 cm. This indicates that increasing the crystal dimension beyond this point does not lead to additional improvement in image fluence. The peak intensity at $D = 4$ cm is approximately 12 times that at $D = 1$ cm, yet it remains unsaturated. In the case of the $R = 400$ mm crystal, neither photon count nor peak intensity shows a saturation trend within the current scope of crystal dimension. At $D = 7$ cm, the peak intensity is about 27 times that at $D = 1$ cm, yet remains unsaturated.

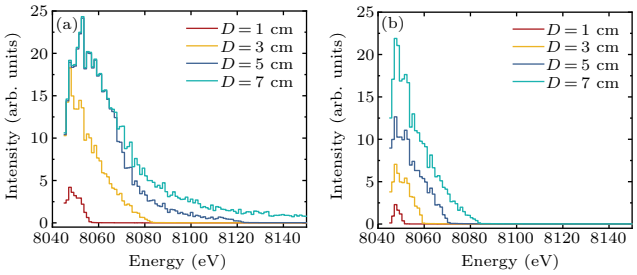


Fig. 4. The diffractable energy spectrum for different crystal dimensions at (a) $R = 200$ mm and (b) $R = 400$ mm in the case of ES.

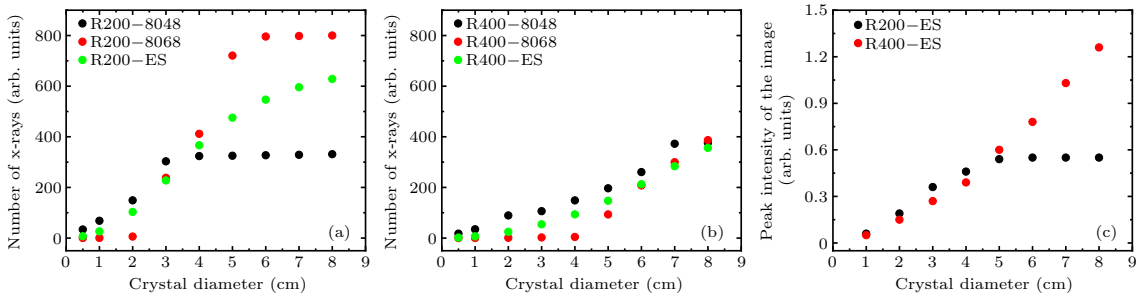


Fig. 5. Photon count on the detector for different crystal dimensions at (a) $R = 200$ mm and (b) $R = 400$ mm. (c) Peak intensities of the image for different crystal dimensions at $R = 200$ mm and $R = 400$ mm (experimental spectrum (ES) were used for the x-ray sources).

4. Effect of crystal dimension on image size and aberration

The simulated image at the detector plane for the x-ray sources with the experimental spectrum is presented in Fig. 6. Figures 6(a)–6(d) depict images of an x-ray source (100 μm FWHM) obtained using crystals with $R = 200$ mm and different crystal sizes, while Figs. 6(e)–6(h) show results for $R = 400$ mm.

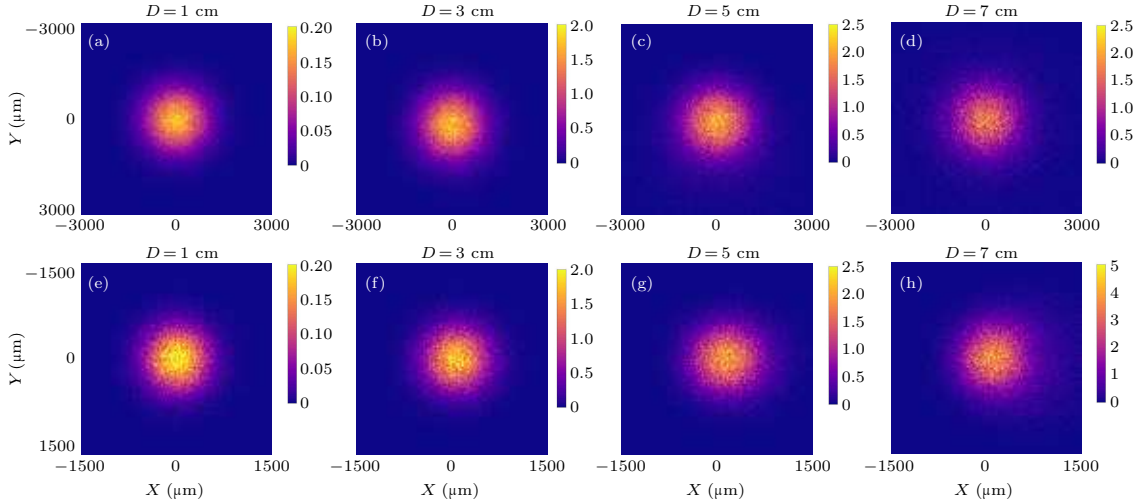


Fig. 6. (a)–(d) The x-ray images of 100 μm Gaussian distributed source using crystals with $R = 200$ mm and varying dimensions in the case of experimental spectrum; (e)–(h) the images using crystals with $R = 400$ mm and varying dimensions in the case of experimental spectrum.

The dimensions of each image spot in Fig. 6, measured in the X and Y directions, are presented in Fig. 7. Figure 7 also includes the dimensions of the image spot for an 8048 eV monoenergetic source. It shows that the image dimension for the 8048 eV monoenergetic source remains relatively constant as the crystal dimension increases, likely due to minimal aber-

ration, maintaining the magnification accuracy. Conversely, in the case of an experimental spectrum x-ray source, the image dimension increases with the crystal dimension due to the broadening of the diffractable energy range and the resulting increase in aberration. Image sizes in both X and Y directions increase with the crystal dimension. Additionally, asymmetry is observed in the images. For crystals with $R = 200$ mm, an asymmetry starts to develop beyond a dimension of 2 cm, with the X dimension slightly larger than the Y dimension by about 3%. When the crystal dimension exceeds 5 cm, the X and Y dimensions become approximately equal. In the case of $R = 400$ mm crystals, significant asymmetry between the X and Y directions emerges for diameters exceeding 3 cm, with the X dimension displaying a more pronounced dispersion, about 9% larger than the Y dimension in the worst situation.

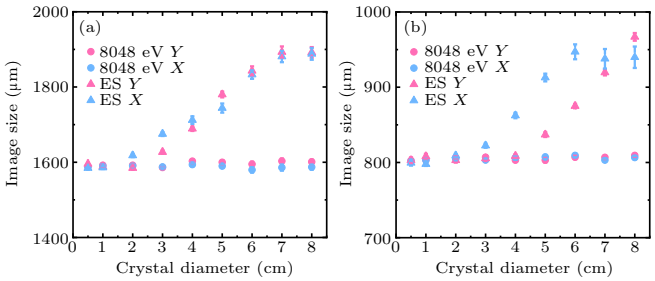


Fig. 7. (a)–(d) The x-ray images of 100 μm Gaussian distributed source using crystals with $R = 200$ mm and varying dimensions in the case of experimental spectrum; (e)–(h) the images using crystals with $R = 400$ mm and varying dimensions in the case of experimental spectrum.

To investigate the reasons for the asymmetry in the X and Y directions, additional simulations have been performed using the crystal dimensions of $D = 5$ cm and $R = 400$ mm to compare the imaging results with 8048 eV, 8068 eV, and the experimental spectrum. The results are shown in Fig. 8. Figures 8(a)–8(c) illustrate the image results for 8048 eV, 8068 eV, and ES, respectively. Figure 8(d) depicts the intensity distributions in the X and Y directions for these images. The image for 8048 eV exhibits mostly symmetrical characteristics in the X and Y directions, with the profile curve centered at the detector, while the 8068 eV images show a notable shift towards the X direction. This shift is primarily due to the fact that the diffraction ring for the 8068 eV is presented on the left of the crystal center in the case of $D = 5$ cm, as shown in Fig. 3. When the experimental spectrum is applied for the x-ray source, all the images with different colors (within the diffractable energy range) and intensities will overlap at the detector plane to form the final image. This leads to an asymmetry in the intensity distribution along the X direction, as illustrated by the green dashed line in Fig. 8(d). As the crystal diameter increases from 3 cm to 6 cm at $R = 400$ mm, the asymmetry in the X and Y directions becomes more pronounced. This exacerbates image distortions and aberrations, potentially hindering the accurate analysis of the images.

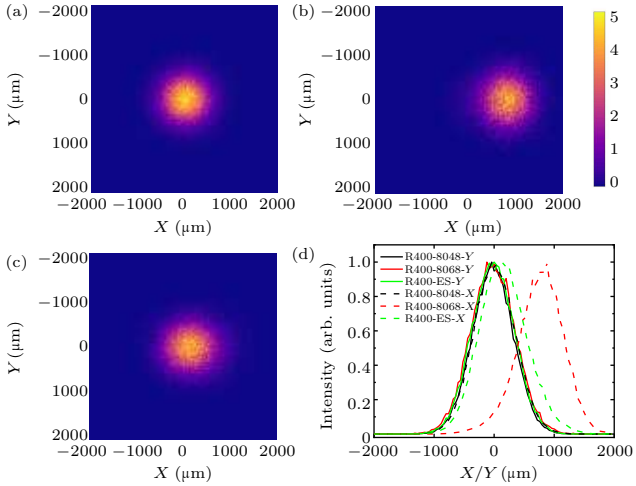


Fig. 8. (a)–(c) Image results of 8048 eV, 8068 eV, and experimental spectrum (ES) on $R = 400$ mm crystals at $D = 5$ cm, respectively. (d) Spatial distributions of image results in the X and Y directions for panels (a)–(c).

5. Effect of crystal dimension on the spatial resolution of imaging systems

Previous works have provided equations for spatial resolution in self-emission imagers. Equation (13) in Ref. [20] involves the crystal aperture 'L', in which case they placed the detector in either the meridional or the sagittal focus. Another choice is to place the detector at the circle of least confusion to yield equal ray aberrations in both directions. As Eqs. (68) and (69) from Ref. [19] define 'w' and 'l' as the effective crystal dimensions in the meridional and sagittal directions, but the specifics were not elaborated upon. The x-ray sources used in our simulations reproduce the energy spectrum from the experiments and cover a specific energy range. In this case, the effective crystal dimension correlates directly with both the crystal dimension and the energy spectrum of the source. We have derived equations to calculate the spatial resolutions for self-emission imager, which explicitly address the dependence of the effective crystal dimension on the energy spectrum and the geometric dimension. We also introduce the novel finding that the spatial resolution varies in meridional and sagittal directions for both the single-energy and experimental spectrum cases.

As illustrated in Fig. 9, the black annual region represents the diffraction range for a specific energy spectrum, assuming an infinitely large crystal. R_1 and R_2 correspond to the radii of the diffraction rings on the crystal for the minimum energy and the maximum energy, respectively. The red circle denotes the curved crystal, with D indicating the geometric diameter. In experiments, the center of the crystal is usually aligned with the 8048 eV diffraction position, which corresponds to the peak of the Cu-$K\alpha$ rays. As the crystal dimension increases, the area and shape of the active diffraction region change accordingly (indicated by the blue area in Fig. 9), fundamentally driving the variability in meridional and sagittal resolu-

tion. From Figs. 9(a)–9(d), as the crystal dimension increases, the effective dimensions of the crystal in the meridional (X direction) and sagittal (Y direction) differ, determining their respective spatial resolutions. The spatial resolutions related to these effective dimensions in the two directions can be described as $\sigma_x = L_x(1-\sin\theta)(\frac{M+1}{M})$, $\sigma_y = L_y(1-\sin\theta)(\frac{M+1}{M})$, respectively.

According to the schematics in Fig. 9, the effective crystal dimension in the meridional direction can be determined as follows:

$$L_x = \begin{cases} \frac{D}{2} + \frac{D}{2}\cos(\alpha), & \text{if } \frac{D}{2} < R_2 - R_1, \\ R_2 - R_1 + \frac{D}{2}\cos(\alpha), & \text{if } R_2 - R_1 < \frac{D}{2} < 2R_1, \\ R_2 - R_1 + \frac{D}{2}, & \text{if } 2R_1 < \frac{D}{2} < R_2 + R_1, \\ 2R_2, & \text{if } R_2 + R_1 < \frac{D}{2}, \end{cases} \quad (1)$$

where D is the crystal dimension, $\alpha = a\cos(\frac{D^2}{2}/(DR_1))$, M is the magnification of the imaging system, and θ is the Bragg diffraction angle corresponding to 8048 eV.

The effective crystal dimension in the sagittal direction can be determined as follows:

$$L_y = \begin{cases} D, & \text{if } \frac{D}{2} < \sqrt{(R_2^2 - R_1^2)}, \\ D\sin(\alpha_1), & \text{if } \sqrt{(R_2^2 - R_1^2)} < \frac{D}{2} < \sqrt{(R_2^2 + R_1^2)}, \\ 2R_2, & \text{if } \sqrt{(R_2^2 + R_1^2)} < \frac{D}{2}, \end{cases} \quad (2)$$

where $\alpha_1 = a\cos((\frac{D^2}{2} + R_1^2 - R_2^2)/(DR_1))$.

In the calculations with the experimental spectrum, R_1 and R_2 represent the radii of the diffraction rings for 8048 eV and 8068 eV, respectively. For $R = 200$ mm, R_2 is calculated to be 1.69 cm and R_1 is 0.74 cm; for $R = 400$ mm, R_2 is 3.67 cm and R_1 is 1.61 cm. The spatial resolution for the experimental spectrum is calculated by incorporating R_1 and R_2 into the relevant equation. Spatial resolution for monoenergetic x-rays across different crystal dimensions is also derived by applying the previous equation, with R_2–R_1 representing the width of the crystal determined by the diffraction curve of the quartz. For $R = 200$ mm, R_2 is 0.94 cm and R_1 is 0.74 cm; for $R = 400$ mm, R_2 is 1.91 cm and R_1 is 1.61 cm. The calculation results, displayed in Figs. 11(a)–11(b), show notable differences in spatial resolution between meridional and sagittal directions for monoenergetic x-ray sources, especially when small crystals are used. The spatial resolution increases in both meridional and sagittal directions as the crystal dimension increases. As the crystal dimension reaches a particular threshold, spatial resolution in both directions peaks (nearly equally) and stabilizes. Notably, the sagittal direction reaches its maximum resolution before the meridional direction. Before peaking, spatial resolution is superior in the meridional direction compared to the sagittal direction.

The spatial resolutions are also obtained through OASYS simulations, as depicted by scatter in Fig. 11. In the simulation, a 100 μm uniformly distributed rectangular source is used along with horizontal or vertical knife edges positioned at the source plane of $Y = 0$ and $X = 0$ to evaluate the spatial resolution by the knife-edge method. Figure 10 displays the knife edge imaging results, positioned at $Y = 0$ μm. Figures 10(a)–10(d) depict the 8048 eV single-energy knife edge simulation results, while Figs. 10(e)–10(h) show results for the experimental spectrum. Figure 10 reveals that both monoenergetic and experimental spectrum knife edges gradually flatten as the crystal dimension increases, signaling a deterioration in spatial resolution. Figure 11 presents comparative results of spatial resolution from equation calculations and knife-edge simulations. Figures 11(a) and 11(c) show results for single-energy and experimental spectrum at $R = 200$ mm, while Figs. 11(b) and 11(d) display the results for $R = 400$ mm. Figure 11 confirms that the spatial resolution calculated by the equation aligns well with that simulated through ray-tracing. With a very small crystal dimension, the spatial resolution can reach a few micrometers. Comparisons of Figs. 11(a) and 11(c) or 11(b) and 11(d) indicate that the difference in spatial resolutions in meridional and sagittal directions remains evident especially in the case of small crystals. Besides, switching from monoenergetic to experimental spectrum worsens the spatial resolution. For monoenergetic x-ray sources, the spatial resolution peaks at approximately 10 μm at $R = 200$ mm and 22 μm at $R = 400$ mm. For the sources with experimental spectrum, the maximum spatial resolution is about 20 μm at $R = 200$ mm and 43 μm at $R = 400$ mm. Meanwhile, the resolution difference between meridional and sagittal directions reduces in the case of the experimental spectrum.

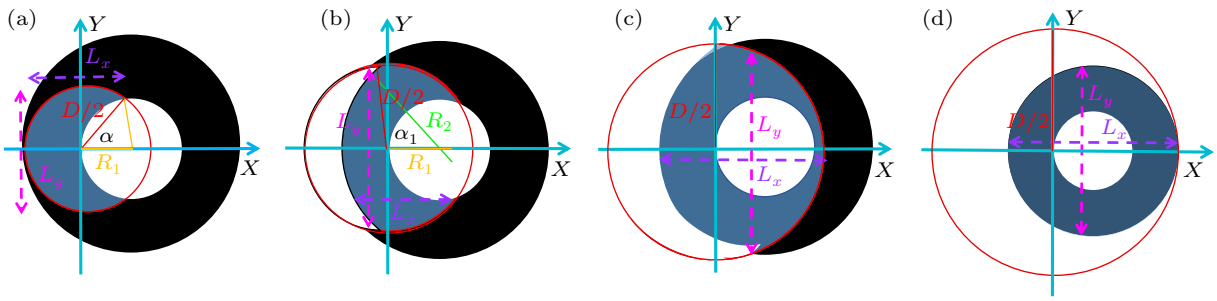


Fig. 9. Effective diffraction area and shape with different crystal dimensions for specific energy spectral ranges.

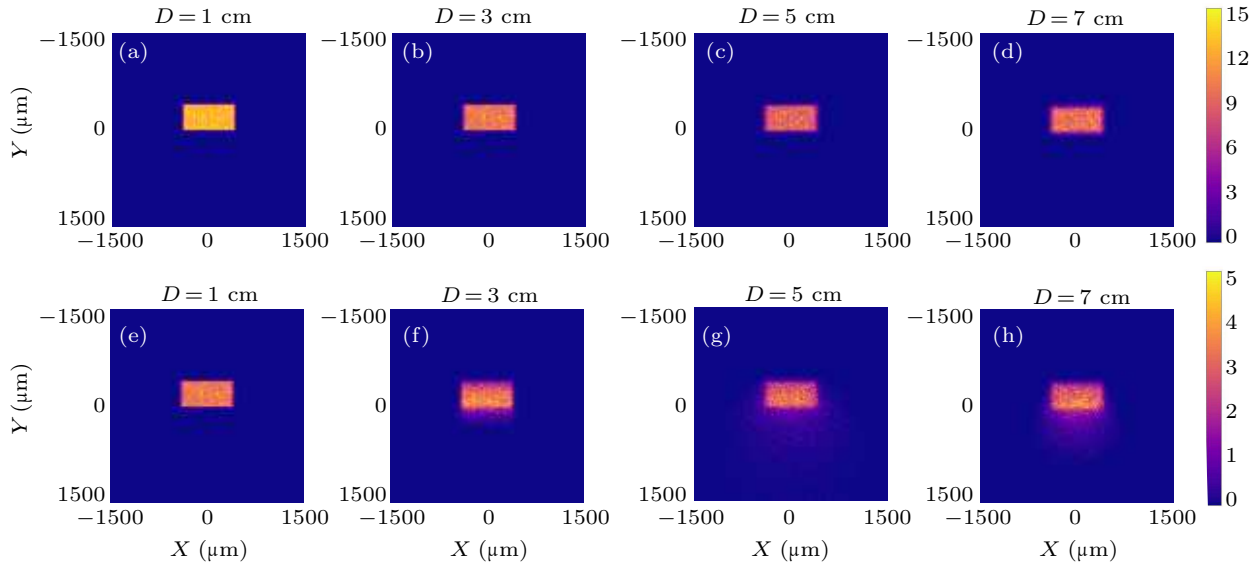


Fig. 10. Knife edge image results at $R = 400$ mm: (a)–(d) 8048 eV results with different crystal dimensions; (e)–(h) experimental spectrum results.

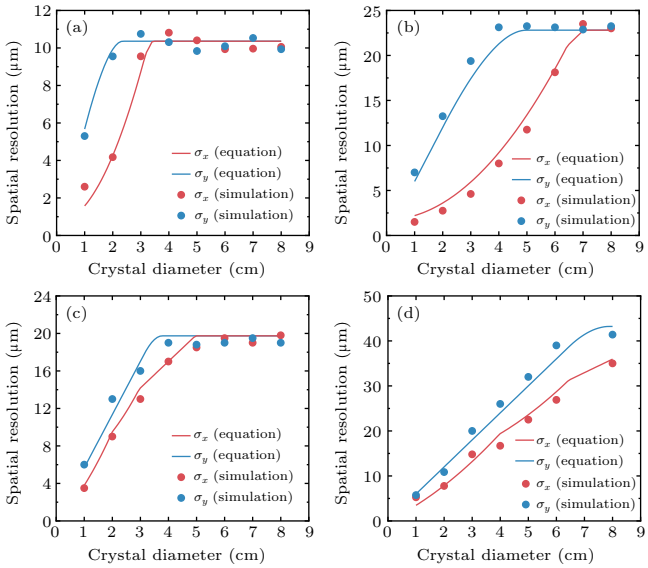


Fig. 11. The spatial resolutions in meridional and sagittal directions obtained from OASYS simulation results and the derivation of the equation, where (a) and (c) are the 8048 eV and experimental spectrum results at $R = 200$ mm; (b) and (d) are the 8048 eV and experimental spectrum results at $R = 400$ mm.

Based on the above simulations, under the current optical design for the spherical crystal self-emission imager, crystals with a curvature of $R = 200$ mm demonstrate superior imaging quality in terms of spatial resolution, image fluence, and image aberration compared to those with $R = 400$ mm. For the $R = 200$ mm imaging system, increasing the crystal dimension beyond 4–5 cm does not substantially improve the image fluence, while the image becomes larger and more blurred. Therefore, enlarging the crystal beyond 4–5 cm is unnecessary if the goal is to improve the image fluence. When the crystal diameter is 4 cm, the image intensity is 12 times that of a 1 cm diameter. The image size remains consistent in the XY directions, with a spatial resolution of approximately 20 μm — four times that at 1 cm. The optimal crystal dimension for a specific experiment should be determined by considering the x-ray source intensity and the required spatial resolution for certain experimental purposes.

6. Conclusion

Using the OASYS ray-tracing code, we conducted the first systematic study on how the crystal dimension affects the performance of a spherical crystal self-emission imager, achieving insightful conclusions. With an $R = 200$ mm crystal imaging system, as the crystal dimension increases, so does the image fluence on the detector plane. Meanwhile, increasing the crystal dimension also leads to image aberration and degradation of spatial resolutions. We have also derived equations for the spatial resolution of the imaging system, which varies with crystal dimension within a specific energy spectrum range, providing expressions for the effective crystal dimension. For the first time, we demonstrated notable variability in spatial resolution of the imaging system across the meridional and sagittal directions. The equation-based calculations, offering guidance for the future design of curved crystal imaging, are in good agreement with the results from the ray-tracing simulations.

Acknowledgment

Project supported by the Strategic Priority Research Program of the Chinese Academy of Sciences (Grant Nos. XDA25051000, XDA25010100, XDA25010300, XDA25030100, and XDA25030200).

References

[1] Kozioziemski B, Bachmann B, Do A, *et al.* 2023 *Rev. Sci. Instrum.* **94** 041102

[2] Belyaev L M, Gil'varg A B, Mikhalov Y A, *et al.* 1976 *Sov. J. Quantum Electron.* **6** 1121
[3] Zhang C L, Zhang Y H, Yuan X H, *et al.* 2024 *Chin. Phys. B* **33** 025201
[4] Harding E C, Robertson G K, Dunham G S, *et al.* 2023 *Rev. Sci. Instrum.* **94** 083509
[5] Lindl J D 1994 *AIP Conference Proceedings* **318** 635
[6] Kodama R, Norreys P A, Mima K, *et al.* 2001 *Nature.* **412** 798
[7] Azechi H, Sakaiya T, Watari T, *et al.* 2009 *Phys. Rev. Lett.* **102** 235002
[8] Betti R, Zhou C D, Anderson K S, *et al.* 2007 *Phys. Rev. Lett.* **98** 155001
[9] Xu Z H, An H W and Wang J J 2024 *Chin. Phys. Lett.* **41** 088201
[10] Wang Z L, Chen Z H, Gu Y, *et al.* 2023 *Chin. Phys. B* **32** 038704
[11] Fujioka S, Fujiwara T, Tanabe M, *et al.* 2010 *Rev. Sci. Instrum.* **81** 10
[12] Koch J A, Aglitskiy Y, Brown C, *et al.* 2003 *Rev. Sci. Instrum.* **74** 2130
[13] Kawaguchi C F, Flippo K A, Rasmus A M, *et al.* 2021 *Rev. Sci. Instrum.* **92** 093508
[14] Theobald W, Solodov A A, Stoeckl C, *et al.* 2014 *Nat. Commun.* **5** 5785
[15] Baton B, Koenig M, Fuchs J, *et al.* 2008 *Phys. Plasmas* **15** 042706
[16] Jarrott L C, McGuffey C, Beg F N, *et al.* 2017 *Phys. Plasmas* **24** 102710
[17] Jarrott L C, Wei M S, McGuffey C, *et al.* 2016 *Nat. Phys.* **12** 499
[18] Ovchinnikov V M, Schumacher D W, McMahon M, *et al.* 2013 *Phys. Rev. Lett.* **110** 065007
[19] Akli K U, Storm M J, McMahon M, *et al.* 2012 *Phys. Rev. E.* **86** 26404
[20] Chawla S, Wei M S, Mishra R, *et al.* 2013 *Phys. Rev. Lett.* **110** 025001
[21] Schollmeier M S, Geissel M, Shores J E, *et al.* 2015 *Appl. Opt.* **54** 5147
[22] Sinars D B, Bennett G R, Wenger D F, *et al.* 2003 *Appl. Opt.* **42** 4059
[23] Zhu J Q, Zhu J, Li X C, *et al.* 2018 *High Power Laser Sci. Eng.* **7** e12
[24] Zhang J, Wang W M, Yang X H, *et al.* 2020 *Phil. Trans. R. Soc. A* **378** 20200015
[25] Rebuffi L and Rio M S D 2017 *Advances in Computational Methods for X-Ray Optics IV Society of Photo-Optical Instrumentation Engineers (SPIE) Conference Series*
[26] Jiang C L, Xu J, Mu B Z, *et al.* 2021 *Opt. Express* **29** 6133
[27] Li Y, Dong J J, Xie Q, *et al.* 2019 *Opt. Express* **27** 8348
[28] Sakata S, Lee S, Morita H, *et al.* 2018 *Nat. Commun.* **9** 3937